Nonhydrostatic and nonlinear contributions to the energy flux budget in nonlinear internal waves

S. K. Venayagamoorthy and O. B. Fringer

Department of Civil and Environmental Engineering, Stanford University, Stanford, California, USA

Received 4 May 2005; revised 28 June 2005; accepted 6 July 2005; published 5 August 2005.

[1] We use high-resolution two-dimensional simulations to model the generation and evolution of nonlinear internal waves formed as a result of the interaction of a first-mode internal wave field with idealized slopes. The derivation of the energy equation and the energy flux terms are presented. By employing an analysis of the distribution of the energy flux across the shelf break, we quantify the contributions to the energy flux budget from nonhydrostatic as well as nonlinear effects in comparison to the contribution from the baroclinic pressure anomaly term used widely for linear internal waves. Our results show that the contributions to the total energy flux from these additional terms are significant in these large nonlinear internal waves, consistent with recent field observations. **Citation:** Venayagamoorthy, S. K., and O. B. Fringer (2005), Nonhydrostatic and nonlinear contributions to the energy flux budget in nonlinear internal waves, *Geophys. Res. Lett.*, *32*, L15603, doi:10.1029/2005GL023432.

1. Introduction

[2] Recent observations in the coastal ocean reveal the ubiquitous nature of nonlinear internal solitary waves [e.g., *Klymak and Moum*, 2003; *Carter et al.*, 2005; *Hosegood et al.*, 2004; *Scotti and Pineda*, 2004]. These authors cite some of the first waves of elevation observed in coastal waters. Very little is known on how and where these waves are generated, though it is hypothesized that the interaction of long-first mode internal tides interacting with bottom topography can be one possible mechanism. These bottom-trapped nonlinear internal waves (herein referred to as NLIWs) are implicated in cross-shelf transport of nutrients, sediments and contaminants, not withstanding their contributions to diapycnal mixing on coastal shelves.

[3] The energy flux through a given location gives a measure of the amount of energy available for mixing/transport elsewhere (e.g. this would be upshelf for an onshore propagating wave) [*MacKinnon and Gregg*, 2003]. The standard approach in energy flux calculations is to only account for the contributions due to the hydrostatic pressure fluctuations given by $p' = P_{SH} + g\int_z^0 \rho' dz'$ where P_{SH} denotes the free-surface pressure and ρ' is the density fluctuations associated with internal waves [see, e.g., *Kunze et al.*, 2002]. However, the contributions to the energy flux due to the vertical inertia of the fluid parcels will be significant in NLIWs since the aspect ratio of these waves is of order one [e.g., see *Carter et al.*, 2005]. The contributions from the nonlinear terms can also be quite significant. Recently, *Scotti and Pineda* [2004] showed that NLIWs observed near the Massachusetts Bay depart strongly from weakly-nonlinear and weakly-nonhydrostatic conditions owing to their steepness, highlighting the need to take into account these effects in the energy flux budget.

[4] In this paper, we present results from high-resolution two-dimensional laboratory-scale simulations modeling the generation and evolution of NLIWs formed as a result of the interaction of a first-mode internal wave field with an idealized sloped coastal shelf. We provide a derivation of all the relevant terms in the energy flux budget and compute these terms in our simulations in order to quantify the contributions from nonhydrostatic pressure as well as nonlinearity. The partitioning of the incident internal wave energy over the course of the interaction process is discussed extensively in a related paper by S. K. Venayagamoorthy and O. B. Fringer (Energetics of the interaction of internal waves with a shelf break, submitted to *Journal of Fluid Mechanics*, 2005).

2. Energy Flux Budget

[5] In this section, we present the evolution equation for the total energy with a discussion of the different terms that contribute to the energy flux budget and how they are computed in the current simulations. Results showing the relative contributions to the energy flux budget follow in Section 3.

2.1. Derivation

[6] The governing Navier-Stokes equations with the Boussinesq approximation are given by

$$\frac{\partial \mathbf{u}}{\partial t} + \mathbf{u}\cdot\nabla\mathbf{u} = -\frac{1}{\rho_0}\nabla p + \nu\nabla^2\mathbf{u} - \frac{g}{\rho_0}\rho\mathbf{k}, \tag{1}$$

$$\frac{\partial \rho}{\partial t} + \nabla\cdot(\rho\mathbf{u}) = \kappa\nabla^2\rho\,, \tag{2}$$

$$\nabla\cdot\mathbf{u} = 0, \tag{3}$$

where ν is the kinematic viscosity and κ is the scalar diffusivity.

[7] The total energy (sum of kinetic and potential energy) is obtained by taking the dot product of equation (1) with $\mathbf{u}$ and multiplying equation (2) by gz and summing the two resulting equations to obtain

$$\frac{\partial}{\partial t}(\rho_0 q + \rho g z) + \nabla\cdot\mathbf{f} = -\rho\epsilon - 2\kappa\frac{\partial}{\partial z}(\rho g)\,, \tag{4}$$

0094-8276/05/2005GL023432$05.00

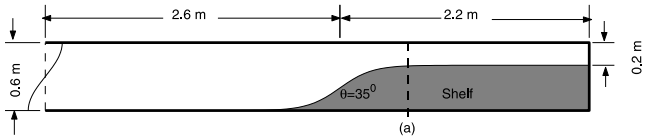

Figure 1. Schematic of the laboratory setup that forms the domain for the current simulations. The buoyancy frequency is $N = 0.57$ rad/s, corresponding to a density difference of $\Delta\rho/\rho_0 = 2\%$ over the depth. Line (a) represents the transect used to compute the energy flux in Section 3.

where $q = \mathbf{u} \cdot \mathbf{u}/2$ is the kinetic energy per unit mass, $\mathbf{f}$ is the total energy flux given by

$$\mathbf{f} = \mathbf{u}(p + \rho g z + \rho_0 q) - \mu \nabla q - \kappa \nabla(\rho g z)\,, \tag{5}$$

and the viscous dissipation rate of kinetic energy is given by $\epsilon = \nu \dfrac{\partial u_i}{\partial x_j}\dfrac{\partial u_i}{\partial x_j}$. For the present analysis we neglect the contribution of the diffusive fluxes of kinetic and potential energies (the last two gradient transport terms in equation (5)) to the energy flux (see, e.g., *Fringer* [2001] for a justification).

[8] The depth-integrated horizontal energy flux at any given vertical section in SI units of W m^{-1}, is then given by

$$F_E = \int_{-d}^{0} u(p + \rho g z + \rho_0 q)\,\mathrm{d}z\,, \tag{6}$$

where u is the onshore (horizontal) velocity. The pressure term p inside the parentheses in equation (6) can be written as the sum of the hydrostatic and nonhydrostatic parts, where the hydrostatic pressure $P_H = P_{SH} - \rho_0 g z + g\int_z^0 \rho_b \mathrm{d}z' + g\int_z^0 \rho' \mathrm{d}z'$, with P_{SH} denoting the free-surface pressure. The last term here represents the hydrostatic pressure fluctuations and accounts for most of the energy flux in linear internal waves (i.e., waves with small aspect ratios). The nonhydrostatic pressure P_{NH} arises due to the vertical inertia in the waves and is given by $P_{NH}(z) = P_{NH}(0) + \rho_0 \int_z^0 \dfrac{Dw}{Dt}\mathrm{d}z'$, where $\dfrac{D}{Dt}$ denotes the total derivative following a fluid parcel. It is easy to show that the contribution to the energy flux from both P_{SH} and $P_{NH}(0)$ integrate to zero since $\int_{-d}^{0} u\mathrm{d}z = 0$. This is convenient in numerical codes using the rigid-lid approximation (e.g. the LES code we use) and allows for the direct computation of the nonhydrostatic contributions to the energy flux budget using the nonhydrostatic pressure that is computed from the pressure-Poisson solver in our code. However, it is important to note that neglecting P_{SH} and $P_{NH}(0)$ will yield incorrect vertical profiles of energy flux [see, e.g., *Kunze et al.*, 2002]. The second term representing contributions from the potential energy in equation (6) can be written as $\rho_0 g z + \rho_b g z + \rho' g z$ (since the total density is $\rho = \rho_0 + \rho_b + \rho'$, where ρ_0 is the reference density, ρ_b is the imposed background density field and ρ' represents the density fluctuations due to internal waves). The last term is the nonlinear contribution (kinetic energy term) and is straightforward to compute numerically. Hence equation (6) (after some simplification) becomes

$$\begin{aligned} F_E = {} & \underbrace{g\int_{-d}^{0} u \int_{z}^{0} \rho'\,\mathrm{d}z'\,\mathrm{d}z''}_{(a)} + \underbrace{\rho_0 \int_{-d}^{0} u \int_{z}^{0} \frac{Dw}{Dt}\,\mathrm{d}z'\,\mathrm{d}z''}_{(b)} \\ & + \underbrace{\rho_0 \int_{-d}^{0} uq\,\mathrm{d}z'}_{(c)} + \underbrace{\int_{-d}^{0} u\rho' g z\,\mathrm{d}z'}_{(d)} + \underbrace{\int_{-d}^{0} u\rho_b g z\,\mathrm{d}z'}_{(e)} \\ & + \underbrace{g\int_{-d}^{0} u \int_{z}^{0} \rho_b\,\mathrm{d}z'\,\mathrm{d}z''}_{(f)}\,. \end{aligned} \tag{7}$$

To summarize, the terms in equation (7) are:

[9] (a) Energy flux due to rate of work done by the hydrostatic pressure fluctuations.

[10] (b) Energy flux due to rate of work done by the nonhydrostatic pressure.

[11] (c) Energy flux due to advection of kinetic energy.

[12] (d) Energy flux from advection of potential energy due to density fluctuations.

[13] (e) Energy flux from advection of potential energy due to the presence of the mean background density field.

[14] (f) Energy flux due to rate of work done by the hydrostatic pressure due to the background density field.

[15] In what follows we compute the contributions from each of the terms shown in equation (7) to the total energy flux at the shelf break (shown in Figure 1) and discuss the relative effects of each term in the energy flux budget.

2.2. Numerical Setup

[16] We solve equations (1)–(3) with the LES code developed by *Fringer and Street* [2003] in the two-dimensional domain shown in Figure 1. This domain is a proposed experimental setup of the companion laboratory-scale experiments for this study. The code uses the method of *Zang et al.* [1994] to solve equations (1)–(3) using a finite volume formulation on a generalized curvilinear coordinate nonstaggered grid with a rigid lid.

[17] We use an initial background linear stratification given by $\dfrac{\rho_b(z)}{\rho_0} = -\dfrac{\Delta\rho}{\rho_0}\left(\dfrac{z}{d}\right)$, with $\dfrac{\Delta\rho}{\rho_0} = 0.02$, which results in a buoyancy frequency of $N = 0.57$ rad s^{-1} in a depth of $d = 60$ cm. A first mode internal wave given by $U(0, z, t) = U_0 \cos(mz)\sin(\omega t)$ is imposed at the left boundary of the domain shown in Figure 1, and U_0 is the velocity amplitude of the forcing, m is the vertical wavenumber corresponding to a mode-1 baroclinic wave with $m = \pi/d$, ω is the forcing frequency, and U is the cross-shore velocity component. Boundary conditions for cross-shore velocity U are no-slip on the bottom wall and free-slip on all other walls. The density and vertical velocity fields are gradient-free at the boundaries. The grid size is 512×128, with a maximum Courant number, $C = \left[\dfrac{|u|}{\Delta X} + \dfrac{|w|}{\Delta Z}\right]\Delta t$, of 0.2. We use a kinematic viscosity of $\nu = 10^{-5}$ m^2 s^{-1}, and scalar diffusivity of $\kappa = 10^{-6}$ m^2 s^{-1}.

3. Results and Discussion

[18] We present results obtained from the interaction of an incident first-mode internal wave with frequency $\omega =$

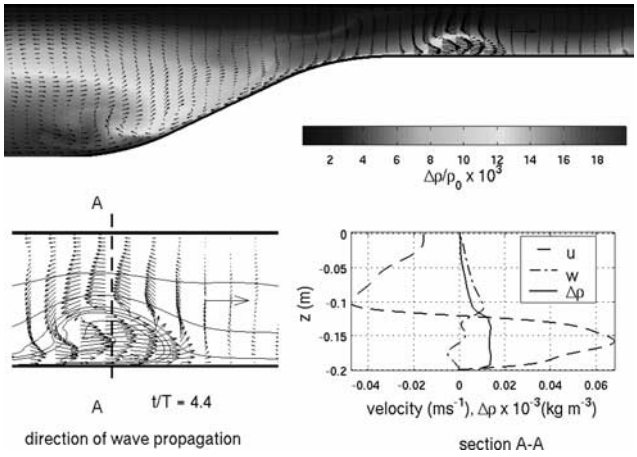

Figure 2. Numerical computation of a breaking internal wave on a critical slope, showing how the solitary bolus propagates onshore as a result of the interaction process. The top panel shows the velocity vectors superimposed on the density profile (shown in color) at time $t/T = 4.4$, with $T = 19.2$ s. The lower left panel shows a detailed view of the internal bolus seen onshelf in the color plot, indicating the amplification of onshore velocities. The magnitude of the single horizontal velocity vector in the right hand center is 10 cm s^{-1} and the forcing velocity amplitude is U_0 = 4 cm s^{-1}. The lower right panel shows the horizontal and vertical velocity profiles with the solid line depicting the density profile with $\Delta\rho$ in kg m^{-3} scaled by 10^{-3}. See color version of this figure in the HTML.

0.328 rad s^{-1} and $U_0 = 4$ cm s^{-1}. For this given frequency, the bottom slope is critical i.e., the ratio $\gamma/s = 1$, where γ is the bathymetric slope and s is the slope of the internal wave energy characteristic, which is defined by

$$s = \tan\alpha = \frac{k}{m} = \left(\frac{\omega^2 - f^2}{N^2 - \omega^2}\right)^{1/2}, \tag{8}$$

where α is the angle of the internal wave characteristic, f is the sine of latitude Coriolis parameter ($f = 0$ for the present simulations), and N is the buoyancy frequency.

3.1. Structure of Bolus

[19] Figure 2 shows the velocity vectors superimposed over the density field and depicts the interaction of a nonlinear first-mode internal wave field with a sloped coastal shelf break in the domain shown in Figure 1. The solitary bolus that propagates onshore is formed from an upslope propagating bolus that forms as a result of the interaction of the incoming wave field with the slope and subsequent ejection of this bolus of heavy fluid onto the shelf. This is consistent with earlier numerical simulation results and laboratory experiments of others [*Slinn and Riley*, 1998; *Legg and Adcroft*, 2003; *Cacchione and Wunsch*, 1974; *Ivey and Nokes*, 1989].

[20] These boluses are self-advecting vortex cores with high aspect ratios that are propelled by some initial momentum and have large onshore velocities contained within their trapped cores (see bottom left panel in Figure 2). Using a simple momentum-viscous balance, the advection speed of the bolus is estimated to be of the order of 5 cm s^{-1} consistent with the observed propagation speed, whereas the expected speed for a gravity current would be about 2 to 3 times higher than this value.

[21] Figure 3 depicts the evolution of the trapped core of the bolus shown in Figure 2. Figure 3 shows the results at six points in time normalized by the wave period $T = 2\pi/\omega$. The loss of mass from the bolus core to the surrounding fluid was estimated by calculating the mass contained between identical isopycnals as the bore evolved in time. The mass of the bolus at $t/T = 5.1$ is about 70 percent of its mass at $t/T = 4.4$, indicating that these boluses can be an important mechanism for transporting and mixing dense ocean water with the relatively homogeneous shelf water.

3.2. Energy Flux Contributions

[22] We compute the depth-integrated energy flux using equation (7) at transect (a) shown in Figure 1. Figure 4 shows the total (contributions from all the terms in equation (7)) depth-integrated flux as a function of time. The fluxes have been normalized by the estimate of the energy flux for an incoming internal wave using linear theory [*Kundu*, 1990], for which

$$F_L = \frac{\rho_0 \omega U_0^2}{2k}\, d, \tag{9}$$

where ρ_0 is the reference density, ω is the forcing frequency, U_0 is the forcing amplitude, d is the offshore depth, $m = \pi/d$ is the vertical wavenumber, and k is the horizontal wavenumber that is readily obtained from the dispersion

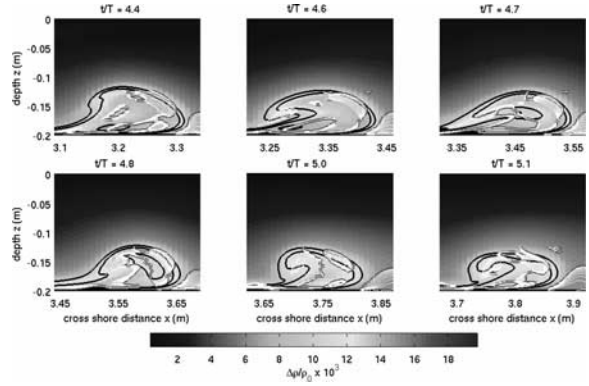

Figure 3. Evolution of an internal bolus as it propagates onshore for critical slope. The color bar shows the density difference $\Delta\rho$. The plots span from non-dimensional t/T = 4.4 to 5.1. The density contours shown in solid black lines are 10, 12 & 14 kg m^{-3} as referenced from ρ_0 = 1000 kg m^{-3} respectively. Also shown are red contours of critical Richardson number, $Ri_c = 0.25$, and white contours of $Ri < Ri_c$. Here $Ri = N^2/\left(\frac{\partial u}{\partial z}\right)^2$, where N is the buoyancy frequency and $\frac{\partial u}{\partial z}$ is the vertical shear rate. See color version of this figure in the HTML.

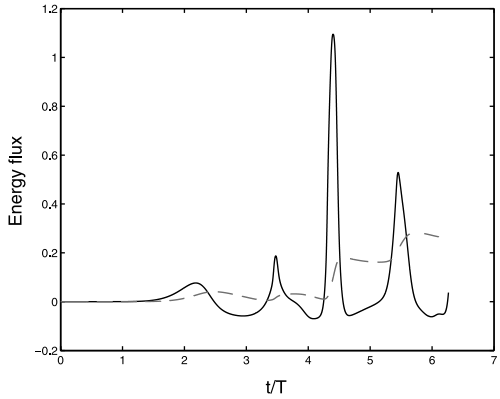

Figure 4. Normalized total energy flux as a function of time t/T at x = 3.2 m, γ/s = 1; solid lines: depth-integrated energy flux F_E; dashed lines: cumulative energy flux E_τ. The intermittent peaks in the depth integrated flux, F_E, signify the passage of internal boluses through transect (a) shown in Figure 1. T = 19.2 s. See color version of this figure in the HTML.

relation for internal waves. Also shown in Figure 4 is the cumulative (time-integrated) energy flux given by

$$E_\tau = \int_0^t F_E(\tau)\, d\tau\,. \tag{10}$$

The cumulative energy fluxes have all been normalized by F_L/ω. The intermittent peaks in the depth-integrated energy flux signify the passage of the nonlinear internal boluses.

[23] The contributions to both the total depth-integrated energy flux and cumulative energy flux from each of the terms in equation (7) are shown in Figure 5 and summarized in Table 1. The hydrostatic pressure anomaly term comprises over 50% of the cumulative energy flux.

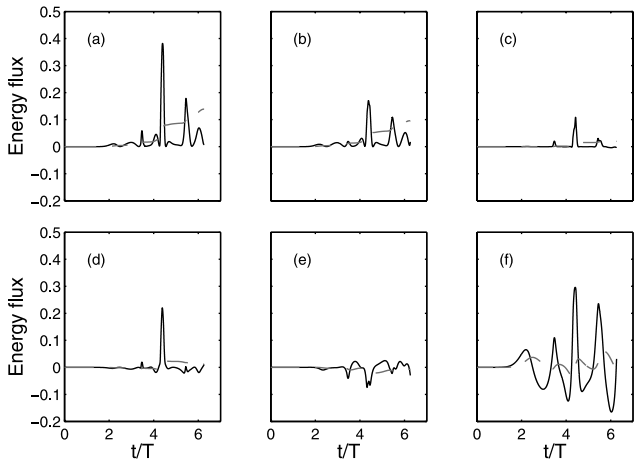

Figure 5. Normalized energy fluxes as a function of time t/T at x = 3.2 m, γ/s = 1; for each of the six terms shown in equation (7) as follows: (a) first term; (b) second term; (c) third term; (d) fourth term; (e) fifth term; (f) sixth term; respectively. Solid lines: depth-integrated energy flux F_E; dashed lines: cumulative energy flux E_τ. See color version of this figure in the HTML.

Table 1. Percentage Contributions of the Terms in Equation (7) to the Total Cumulative Energy Flux E_τ

Term (in Equation (7))	Contribution (percent)	Ratio (Relative to Hydrostatic Term (1))
(a) Hydrostatic pressure anomaly term	54	1.00
(b) Nonhydrostatic pressure term	37	0.69
(c) KE term	8	0.14
(d) PE (density anomaly) term	4	0.09
(e) PE (due to ρ_b) term	−3	0.05
(f) Hydrostatic pressure (due to ρ_b) term	0	0.005

The nonhydrostatic pressure term contribution is about 35%. The contributions from both the advective flux of potential energy due to density fluctuations and the nonlinear advection of kinetic energy account for approximately 10% of the cumulative energy flux. The background density terms (i.e. terms 5 and 6 in Table 1) have negligible contributions to the cumulative energy flux. However, they are important in the instantaneous sense as shown in Figure 5.

[24] The contributions of all the other terms relative to the hydrostatic pressure anomaly term is also given in Table 1. The only important term besides the usually computed hydrostatic pressure anomaly term is the nonhydrostatic pressure term. These results highlight the importance of accounting for the vertical inertia in highly nonlinear internal waves.

4. Conclusions

[25] We have presented results from high-resolution two-dimensional laboratory-scale simulations of internal waves interacting with a sloped coastal shelf break, leading to the formation of boluses that propagate onshore. These boluses are both highly nonlinear and nonhydrostatic due to their steepness and enhanced velocities within their trapped cores. We have presented calculations of the energy flux that clearly show the need to include the contributions from the nonhydrostatic pressure as well as the nonlinear terms in the calculation of the total energy flux in these boluses.

[26] As indicated by many others [*Klymak and Moum*, 2003; *Scotti and Pineda*, 2004; *Carter et al.*, 2005], it is critical to understand how NLIWs form, how far onshore they propagate and their eventual fate. Answers to some of these fundamental questions require a better understanding of these waves. This can be attained through detailed field-campaign studies in conjunction with three-dimensional numerical modeling efforts. Our current work is focusing on three-dimensional large-eddy simulations of the internal boluses presented here.

[27] **Acknowledgments.** The authors gratefully acknowledge the support of the Leavell Family Faculty Scholarship in the Department of Civil and Environmental Engineering at Stanford University. We thank Steve Armfield, Jim Moum, Jonathan Nash and Kraig Winters for helpful discussions. The comments of two anonymous reviewers were very helpful in revising the original manuscript.

References

Cacchione, D., and C. Wunsch (1974), Experimental study of internal waves over a slope, *J. Fluid Mech.*, *66*, 223–239.

Carter, G. S., M. C. Gregg, and R.-C. Lien (2005), Internal waves, solitary waves, and mixing on the Monterey Bay shelf, *Cont. Shelf Res.*, *25*, 1499–1520.

Fringer, O. B. (2001), Numerical simulations of breaking interfacial waves, Ph.D. thesis, Stanford Univ., Stanford, Calif.

Fringer, O. B., and R. L. Street (2003), The dynamics of breaking progressive interfacial waves, *J. Fluid Mech.*, *494*, 319–353.

Hosegood, P., J. Bonnin, and H. van Haren (2004), Solibore-induced sediment resuspension in the Faeroe-Shetland Channel, *Geophys. Res. Lett.*, *31*, L09301, doi:10.1029/2004GL019544.

Ivey, G. N., and R. I. Nokes (1989), Vertical mixing due to the breaking of critical internal waves on sloping boundaries, *J. Fluid Mech.*, *204*, 479–500.

Klymak, J. M., and J. N. Moum (2003), Internal solitary waves of elevation advancing on a shoaling shelf, *Geophys. Res. Lett.*, *30*(20), 2045, doi:10.1029/2003GL017706.

Kundu, P. K. (1990), *Fluid Mechanics*, Elsevier, New York.

Kunze, E., L. K. Rosenfeld, G. S. Carter, and M. C. Gregg (2002), Internal waves in Monterey Submarine Canyon, *J. Phys. Oceanogr.*, *32*, 1890–1913.

Legg, S., and A. Adcroft (2003), Internal wave breaking at concave and convex continental slopes, *J. Phys. Oceanogr.*, *33*, 2224–2246.

MacKinnon, J. A., and M. C. Gregg (2003), Mixing on the late summer new england shelf-solibores, shear, and stratification, *J. Phys. Oceanogr.*, *33*, 1476–1492.

Scotti, A., and J. Pineda (2004), Observations of very large and steep internal waves of elevation near the Massachusetts coast, *Geophys. Res. Lett.*, *31*, L22307, doi:10.1029/2004GL021052.

Slinn, D. N., and J. J. Riley (1998), Turbulent dynamics of a critically reflecting internal gravity wave, *Theor. Comput. Fluid Dyn.*, *11*, 281–303.

Zang, Y., R. L. Street, and J. R. Koseff (1994), A non-staggered grid, fractional step method for time-dependent incompressible Navier-Stokes equations in curvilinear coordinates, *J. Comput. Phys.*, *114*, 18–33.

O. B. Fringer and S. K. Venayagamoorthy, Department of Civil and Environmental Engineering, Stanford University, Stanford, CA 94305-4020, USA. (fringer@stanford.edu; vskaran@stanford.edu)